The Effect of the Ambient Solar Wind Medium on a CME-driven Shock and the Associated Gradual Solar Energetic Particle Event

Nicolas Wijsen[1,2] , David Lario[1] , Beatriz Sánchez-Cano[3] , Immanuel C. Jebaraj[4] , Nina Dresing[5] , Ian G. Richardson[1,2] ,
Angels Aran[6] , Athanasios Kouloumvakos[7] , Zheyi Ding[4] , Antonio Niemela[4,8] , Erika Palmerio[9] ,
Fernando Carcaboso[1,10] , Rami Vainio[5] , Alexandr Afanasiev[5] , Marco Pinto[11] , Daniel Pacheco[12] ,
Stefaan Poedts[4,13] , and Daniel Heyner[14]

[1] Heliophysics Science Division, NASA Goddard Space Flight Center, Greenbelt, MD 20771, USA; nicolas.p.wijsen@nasa.gov
[2] Department of Astronomy, University of Maryland College Park, MD 20742, USA
[3] School of Physics and Astronomy, University of Leicester, Leicester, LE1 7RH, UK
[4] Centre for mathematical Plasma-Astrophysics, KU Leuven, B-3001 Leuven, Belgium
[5] Department of Physics and Astronomy, University of Turku, FI-20500 Turku, Finland
[6] Dep. Física Quàntica i Astrofísica. Institut de Ciències del Cosmos (ICCUB), Universitat de Barcelona (UB-IEEC), E-08028 Barcelona, Spain
[7] The Johns Hopkins University Applied Physics Laboratory, Laurel, MD 20723, USA
[8] Solar-Terrestrial Centre of Excellence—SIDC, Royal Observatory of Belgium, B-1180 Brussels, Belgium
[9] Predictive Science Inc., San Diego, CA 92121, USA
[10] Physics Department, The Catholic University of America, Washington, DC 20064, USA
[11] European Space Research and Technology Centre, European Space Agency, 2201 AZ Noordwijk, The Netherlands
[12] Institut für Experimentelle und Angewandte Physik, Christian-Albrechts-Universität zu Kiel, D-24118 Kiel, Germany
[13] Uniwersytet Marii Curie-Skłodowskiej, 20-400 Lublin, Lubelskie, Poland
[14] Institut für Geophysik und extraterrestrische Physik, Technische Universität Braunschweig, D-38106 Braunschweig, Germany

Abstract

We present simulation results of a gradual solar energetic particle (SEP) event detected on 2021 October 9 by multiple spacecraft, including BepiColombo (Bepi) and near-Earth spacecraft such as the Advanced Composition Explorer (ACE). A peculiarity of this event is that the presence of a high-speed stream (HSS) affected the low-energy ion component ($\lesssim 5$ MeV) of the gradual SEP event at both Bepi and ACE, despite the HSS having only a modest solar wind speed increase. Using the EUHFORIA (European Heliospheric FORecasting Information Asset) magnetohydrodynamic model, we replicate the solar wind during the event and the coronal mass ejection (CME) that generated it. We then combine these results with the energetic particle transport model PARADISE (PArticle Radiation Asset Directed at Interplanetary Space Exploration). We find that the structure of the CME-driven shock was affected by the nonuniform solar wind, especially near the HSS, resulting in a shock wave front with strong variations in its properties such as its compression ratio and obliquity. By scaling the emission of energetic particles from the shock to the solar wind compression at the shock, an excellent match between the PARADISE simulation and in situ measurements of $\lesssim 5$ MeV ions is obtained. Our modeling shows that the intricate intensity variations observed at both ACE and Bepi were influenced by the nonuniform emission of energetic particles from the deformed shock wave and demonstrates the influence of even modest background solar wind structures on the development of SEP events.

Unified Astronomy Thesaurus concepts: Solar energetic particles (1491); Solar coronal mass ejections (310); Solar wind (1534); Interplanetary shocks (829)

Supporting material: animations

1. Introduction

When solar energetic particles (SEPs) escape from their acceleration site, they propagate through the solar wind and may eventually be detected in situ by particle detectors on board spacecraft. Since SEPs tend to follow the interplanetary magnetic field (IMF) configuration, a prompt onset in the SEP intensity–time profiles indicates a good magnetic connection between the spacecraft and the SEP source, which is usually located west of the spacecraft due to the nominal spiral shape of the IMF lines (e.g., Cane et al. 1988). However, the occurrence of SEP events in a disturbed interplanetary medium renders the association between the observed intensity enhancements and the SEP source more difficult.

Although most SEP models assume a nominal Parker spiral magnetic field (e.g., Whitman et al. 2022), the presence of intervening solar wind structures may modify the configuration of the magnetic field. Such structures include interplanetary coronal mass ejections (ICMEs), stream interaction regions (SIRs), and folds in the tilted heliospheric current sheet (HCS), among others (e.g., Richardson & Cane 1996; Kallenrode & Cliver 2001; Smith 2001; Bieber et al. 2002; Richardson 2004; Masson et al. 2012; Lario & Karelitz 2014; Richardson 2018; Palmerio et al. 2021). Apart from modifying the IMF geometry, the magnetic field distortions caused by these structures can affect the transport of SEPs by, for example, creating magnetic reflection regions and altering the nominal path length followed by the particles (e.g., Bieber et al. 2002; Wijsen et al. 2020). Interplanetary structures can also have a direct impact on the

turbulence in the medium through which the SEPs propagate (e.g., Smith et al. 2011; Kilpua et al. 2020). Moreover, the characteristics of the shock waves propelled by fast CMEs, which often continuously accelerate energetic particles as they propagate away from the Sun, can be altered by the intervening structures encountered upstream (e.g., Odstrcil & Pizzo 1999; Case et al. 2008; Richardson & Cane 2010). The interaction between a shock and these aforementioned intervening structures may alter the shock properties, which can affect the particle acceleration efficiency and, consequently, modify the time profiles of the energetic particle intensities measured by spacecraft. These energetic particle enhancements are known as gradual SEP events, and include all energetic particles accelerated by the shock driven by a CME as it travels through interplanetary space (e.g., Reames 1999; Desai & Giacalone 2016). The nonuniformity of the solar wind medium can create a variety of SEP intensity–time profiles, each with unique characteristics to understand.

An intricate SEP event where such intervening structures played a fundamental role in the in situ energetic particle measurements occurred on 2021 October 9. The observational characteristics of this event were studied in detail by Lario et al. (2022). The SEPs associated with this eruptive event, which included protons up to ∼100 MeV, were detected by various spacecraft, including Solar Orbiter (Müller et al. 2020), Parker Solar Probe (Fox et al. 2016), BepiColombo (Bepi; Benkhoff et al. 2021), the Solar Terrestrial Relations Observatory Ahead (STEREO-A; Kaiser et al. 2008), the Advanced Composition Explorer (ACE; Stone et al. 1998), and the Wind spacecraft (Wilson et al. 2021, and references therein). These spacecraft were located in a narrow range of longitudes extending from 48° east to 2° west of Earth and at heliocentric distances from 0.33 to 1 au. The solar eruptive event producing the SEPs included a CME and an M1.6-class solar flare in soft X-rays (2B in Hα) that originated from the NOAA Active Region 12882, located at N17°E09°. Hence, the spacecraft were well located close to the longitude of the solar event. The electron event and the associated radio emission were studied in detail by Jebaraj et al. (2023).

One of the main conclusions of Lario et al. (2022) was that the intensity–time profiles of the energetic ions measured at Bepi (located at 0.33 au) as well as ACE and Wind (both at L1) were strongly affected by an intervening high-speed stream (HSS), despite the fact that the HSS was characterized by only a modest gradual increase in the solar wind speed from ∼300 to 410 km s^{-1} at the Sun-Earth Lagrangian point L1. This modest gradual increase in the solar wind speed and the absence of shock waves bounding the SIR generated by the HSS suggest that the SIR alone did not significantly contribute to the acceleration of the observed energetic particles. This is supported by the fact that STEREO-A (at 30° East of Earth) detected only a marginal increase (less than a factor of two) in suprathermal (⩽350 keV) proton intensities when the SIR crossed the spacecraft on October 7, before the SEP event occurred. Furthermore, intensities observed near Earth during the SEP event modeled here were significantly higher than those typically seen during pure SIR events (e.g., Lee et al. 2010), indicating that the event was indeed an SEP and not an SIR event.

During the onset of the SEP event, Bepi and the spacecraft at L1, separated by 0.67 au, were approximately radially aligned and thus on different nominal spiral magnetic field lines.

Nevertheless, both Bepi and the L1 spacecraft measured similarly shaped intensity–time profiles for ion energies ⩽5 MeV. Lario et al. (2022) suggested that the SEP intensity–time profiles observed at Bepi and ACE or Wind could be the result of particles being confined between the SIR driven by the HSS and the CME that generated the SEP event. In this work, we build on the study of Lario et al. (2022) by further exploring the impact of the intervening HSS on the low-energy component (⩽5 MeV) of the gradual SEP event observed by Bepi and near-Earth spacecraft. To do so, we use a modeling approach that combines the particle transport code "PArticle Radiation Asset Directed at Interplanetary Space Exploration" (PARADISE; Wijsen et al. 2019; Wijsen 2020) with the data-driven solar wind and CME propagation model "EUropean Heliospheric FORcasting Information Asset" (EUHFORIA; Pomoell & Poedts 2018; Poedts et al. 2020). Since the inner boundary of EUHFORIA is located at 21.5 solar radii, we do not model particles accelerated early in the SEP event, including high-energy protons, which are presumably mostly accelerated when the shock is still close to the Sun (e.g., Gopalswamy et al. 2005; Reames 2009a, 2009b). Rather, we focus on protons with energies ⩽5 MeV and assume that most of these protons observed by near-Earth spacecraft and Bepi are produced by the shock at larger heliocentric distances, when these spacecraft are magnetically connected with the shock front (Lario et al. 2022).

The EUHFORIA simulation indicates that the large-scale structure of the shock wave driven by the CME as well as the CME itself were strongly deformed due to the nonuniform upstream solar wind conditions. This, in turn, led to a shock wave with strongly varying properties, such as its obliquity and compression ratio. By assuming that the SEP production is proportional to the compression of the shock wave, a good match is found between the observations and the simulation for ⩽5 MeV protons. This suggests that acceleration processes at the shock driven by the ICME may have played a predominant role in shaping the intensity–time profiles of the low-energy component of the gradual SEP event at Bepi and near Earth. It also demonstrates the importance of having realistic models for the solar wind and CME-driven shocks when trying to understand SEP events, as noted in previous studies (e.g., Lario et al. 2017; Kouloumvakos et al. 2022).

The paper is structured as follows. In Section 2, we present the EUHFORIA simulation of the ambient solar wind and the CME. In particular, we emphasize how the modeled CME-driven shock was strongly deformed. Section 3 provides the results of the PARADISE simulation, and a comparison between the observations and the simulations is presented. Section 4 summarizes the main results of the present work.

2. The Solar Wind and Shock Deformation

Figure 1 shows a snapshot of the solar wind speed as obtained from the EUHFORIA simulation in, from left to right, the solar equatorial plane, a meridional slice containing Earth (indicated by a red circle), and a longitudinal versus latitudinal surface at $r = 1$ au. Figure 2 shows the same snapshot as Figure 1, but for the scaled number density instead of the solar wind speed. The synoptic magnetogram and the solar wind speed map at 0.1 au used as input for the EUHFORIA simulation of the background solar wind is shown in Figure 3 of Lario et al. (2022). In Figure 1, the intervening HSS can be seen arriving at Earth at the time of this snapshot (2021
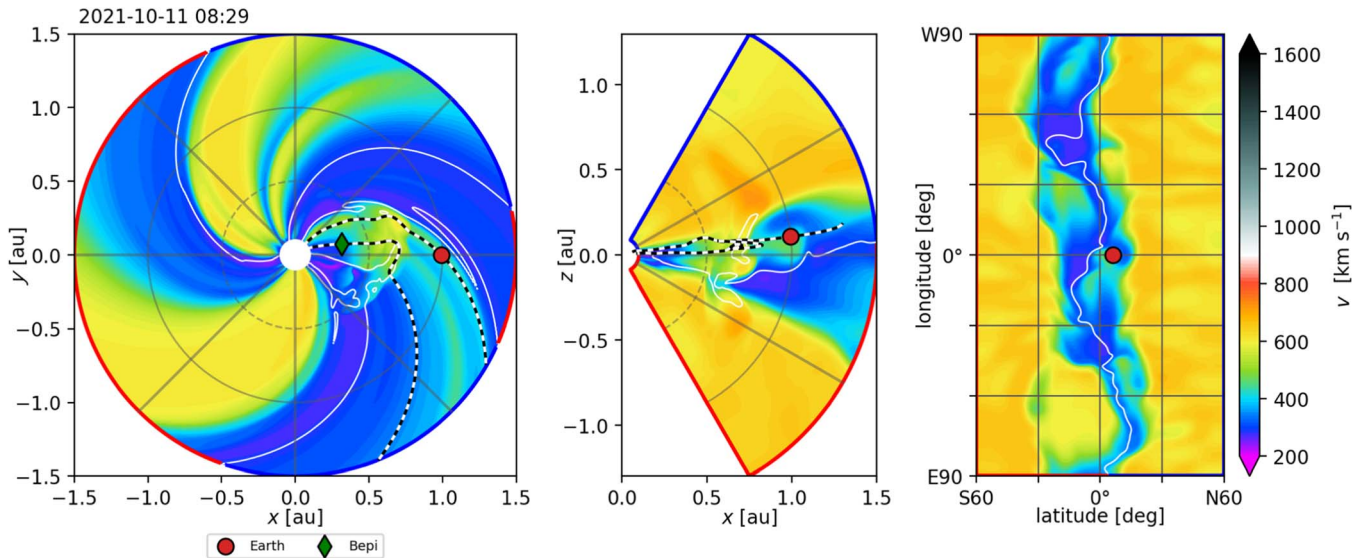
Figure 1. Snapshot (at 2021 October 11, 08:29 UT) of the solar wind speed modeled with EUHFORIA. From left to right, the panels show the solar equatorial plane, the meridional slice containing Earth (red circle), and a slice at $r = 1$ au. The black-white dashed lines are projected magnetic field lines connecting to Earth and to Bepi (green diamond) and the thin white lines indicate the heliospheric current sheet. An animated version of this figure is available, showing the modeled solar wind speed from 2021 October 8 21:59 to 2021 October 14 09:58. The video illustrates how the CME gradually deforms as it propagates through the solar wind, due to the varying upstream solar wind conditions. The real-time duration of the animation is 11 s.

(An animation of this figure is available.)

October 11, 08:29 UT). The density enhancement that has just passed Earth in the left and middle panel of Figure 2 is the SIR produced by this HSS. In addition, both figures show the CME propagating from the Sun toward Earth at $\sim$0.6 au (where the speed and density show a sudden increase). The CME is simulated using EUHFORIA's cone model, which consists of a hydrodynamic cloud of plasma of elevated density and temperature that is inserted into the solar wind with a constant speed and angular width (e.g., Scolini et al. 2018). The insertion parameters of the cone CME are presented in Table 1. For the CME's density and temperature, EUHFORIA's default parameters (see Pomoell & Poedts 2018) were used and the kinematic insertion parameters were chosen by slightly adjusting the shock fitting results presented in Lario et al. (2022), so that the modeled and observed arrival times of the CME shock at Earth match (see also Figure 3).

What is evident from Figures 1 and 2 is that the modeled CME (and its shock wave) was distorted during its propagation through the inner heliosphere. This distortion can be attributed to the varying solar wind conditions upstream of the CME (e.g., Savani et al. 2010; Owens et al. 2017). That is, the portions of the CME propagating through the HSS are less decelerated than the portions propagating through the slow solar wind trailing and preceding the HSS. This is because the larger density and the slower speed of the slow solar wind lead to a drag force acting on the CME that is greater than in the fast solar wind.

To further illustrate the deformation of the CME, we show in Figure 4 a meridional slice showing the ambient solar wind speed together with the shock wave front of the CME, which was obtained using EUHFORIA's shock tracer (see Wijsen et al. 2022, for details). The panels show the western flank of the CME, which is the flank to which Earth is magnetically connected when the CME propagates away from the Sun. The magnetic field line connecting Earth (white circle) with the shock is shown as a white line. The figure illustrates how the

nonuniform upstream solar wind conditions, in addition to deforming the shock surface, also cause the shock to have strongly varying properties. In panel (a), the shock surface is color coded according to the upstream solar wind speed, with the HSS affecting the shock surface. In panel (b) of Figure 4, the shock surface is color coded according to its gas compression ratio r_g, that is, the ratio between the downstream and upstream plasma density (black-orange color bar). Where the surface is colored black, the CME's propagation speed is lower than the local upstream fast magnetosonic speed and hence in those regions the depicted surface is not a shock wave. This occurs mostly in the fast wind originating from the highest northern and southern latitudes. Similarly, it can be seen that where the shock is propagating through the HSS, the compression ratio is $r_g \lesssim 2$ (black-reddish), whereas in the preceding and trailing slow wind, the compression ratio is $r_g \gtrsim 2.5$ (yellowish).

In panel (c) of Figure 4, the shock is color coded according to the shock obliquity θ_{B_n}, which is defined as the angle between the upstream magnetic field and the shock normal (blue-red color bar). A classic cartoon representation assumed for a CME propagating through a uniform solar wind shows that the shock obliquity smoothly varies from a quasi-perpendicular geometry on the west flank of the CME to a quasi-parallel geometry on the east flank of the CME (e.g., Figure 11 in Sarris et al. 1984 or Figure 6 in Zank et al. 2006). This is because it is assumed that (1) the IMF has the same spiral shape everywhere, and (2) the CME does not show a markedly deformation, apart from some flattening, provided that there are no large inhomogeneities present in the CME itself. Both these properties break down once the ambient medium through which the CME propagates is no longer uniform, in which case the shock obliquity is less well behaved. This is because the deformation of the shock wave changes the curvature of the shock front locally, which in turn modifies the shock's local obliquity. This is illustrated in panel (c) of
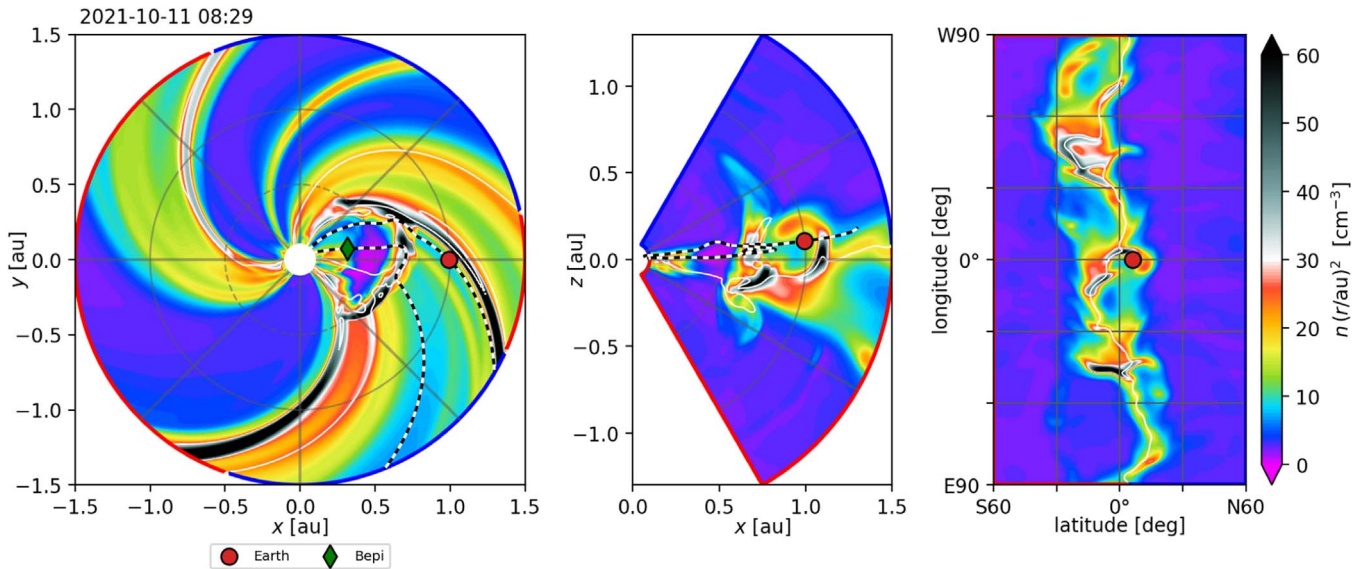
Figure 2. Same as Figure 1, but showing the scaled number density. An animated version of this figure is also available, which depicts the scaled solar wind number density from 2021 October 8 21:59 to 2021 October 14 09:58. The video shows how a nonuniform density distribution downstream of the shock is produced by varying upstream solar wind conditions. The real-time duration of the animation is 11 s.

(An animation of this figure is available.)

Table 1
Input Parameters of the Cone CME Model in the EUHFORIA Simulation

Parameter	Value
Insertion time	2021 Oct 9 at 10:30 UT
Insertion speed	650 km s^{-1}
Insertion longitude (HEEQ)	0°
Insertion latitude (HEEQ)	6°
Half width	45°
Density	10^{-18} kg m^{-3}
Temperature	8 × 10^5 K

Figure 4, where it can be seen that the west flank of the shock contains both quasi-parallel and quasi-perpendicular regions because of its deformation. Likewise, the eastern flank also contains a mix of both quasi-perpendicular and quasi-parallel geometries (not shown).

3. Energetic Particles at Earth and Bepi

3.1. PARADISE Set-up

Next, we use PARADISE (Wijsen 2020) to model the temporal and spatial evolution of an energetic proton population propagating through the EUHFORIA solar wind configuration presented in the previous section. PARADISE does this by solving the five-dimensional focused transport equation (FTE; see, e.g., van den Berg et al. 2020, for a recent review) by integrating an equivalent set of Itô-stochastic equations forward in time. The resulting pseudo-particles are sampled on a spherical mesh of radial resolution $dr = 0.02$ au and angular resolution $d\varphi = d\vartheta = 1°$, where φ and ϑ denote the azimuthal and latitudinal coordinates, respectively. The solution obtained by the model is the directional differential intensity. The FTE solved by PARADISE takes into account the effects of solar wind turbulence by including a diffusion process in the particles' pitch-angle coordinate and a spatial diffusion process perpendicular to the average IMF. For details on the

implementation of PARADISE, we refer to Wijsen (2020). In the work presented here, we use standard quasi-linear theory (QLT; Jokipii 1966) to prescribe the pitch-angle diffusion coefficient and assume that the protons propagate with a parallel mean free path $\lambda_{\parallel} = 0.3(R/R_0)^{2-q}$ au, where $q = 5/3$ is the spectral index of a Kolmogorov turbulence spectrum, R is the particle rigidity, and $R_0 = 43$ *MV*, which corresponds to the rigidity of a 1 MeV proton. The resulting values for $\lambda_{\parallel}$ fall toward the higher end of the range of parallel mean free paths usually derived from observations (e.g., Bieber et al. 1994). In the PARADISE simulation, particle distributions are also subject to a cross-field diffusion process, characterized by a constant perpendicular mean free path $\lambda_{\perp} = 3 \times 10^{-4}$ au. The assumption that $\lambda_{\perp}/\lambda_{\parallel} \sim 10^{-3}$ means that the energetic protons are predominantly propagating along the IMF lines in the simulation.

In our simulation, protons with energies between 50 keV and 6 MeV are continuously injected along the entire shock wave. This is done by introducing the following source function in the FTE solved with PARADISE (e.g., Prinsloo et al. 2019; Wijsen et al. 2022):

$$Q(E) = C|\nabla \cdot V_{\text{sw}}|(E_0/E)^3(r_0/r)^2, \qquad (1)$$

where C is a normalization factor with the units of differential intensity (cm^{-2} MeV^{-1} s^{-1} sr^{-1}), E is the proton energy, and V_{sw} is the solar wind velocity vector. The reference values E_0 and r_0 are chosen as 88 keV and 1 au, respectively The divergence of the solar wind velocity vector appearing in Equation (1) measures the rate of the compression/expansion of the solar wind in units of s^{-1}. Despite prevalent particle acceleration theories, such as diffusive shock acceleration (DSA; e.g., Bell 1978; Drury & Voelk 1981) and shock drift acceleration (SDA; e.g., Ball & Melrose 2001, and references therein), suggesting a dependence on θ_{B_n}, our injection rate Q does not consider it explicitly. This is partly due to the incomplete understanding of the exact relation between θ_{B_n} and
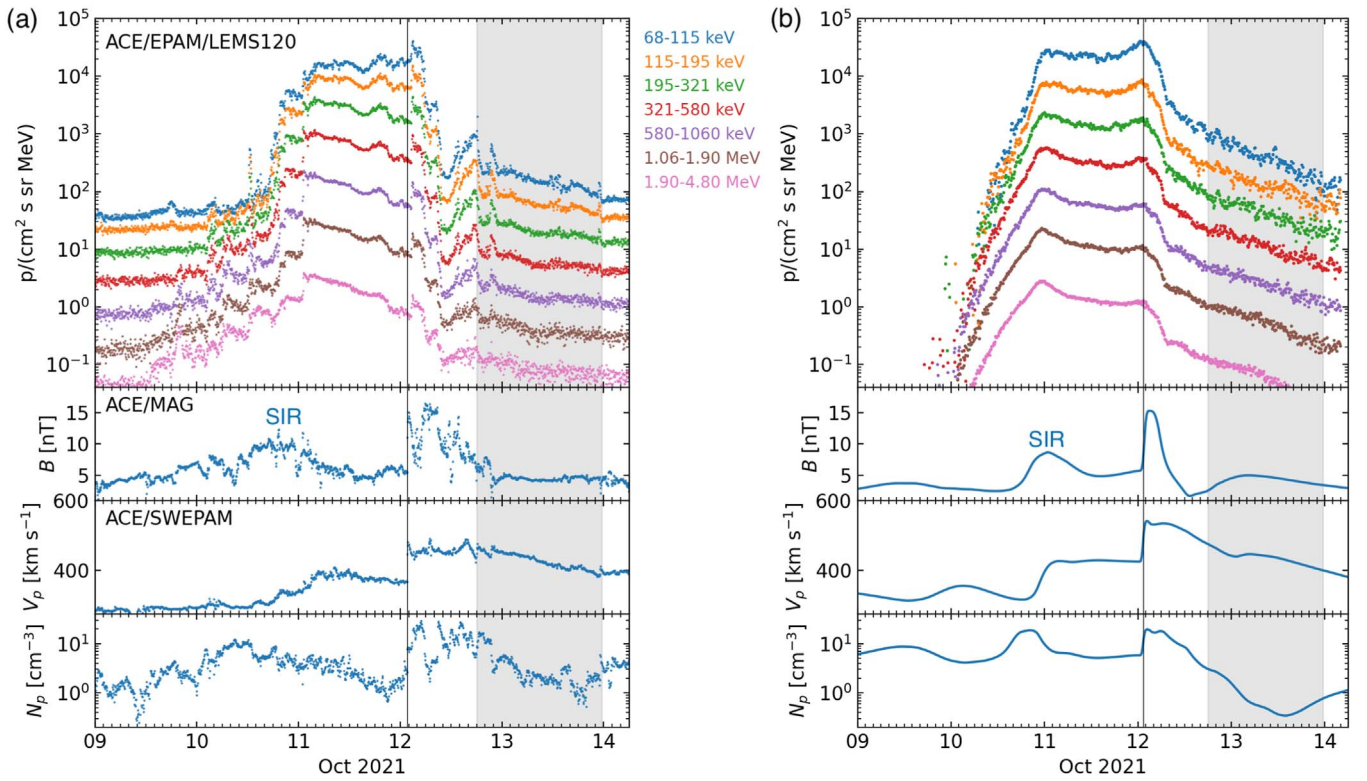
Figure 3. Observed (panel a) and modeled (panel b) SEP intensities and solar wind properties at ACE. From top to bottom, the panels show the SEP intensities for different energy channels spanning 68 keV–4.8 MeV, the magnetic field magnitude, the solar wind speed, and the proton density. The vertical line indicates the shock arrival time and the gray shaded region indicates the magnetic cloud as identified by Lario et al. (2022).

the ongoing particle acceleration mechanism, and partly because our simulation reproduce the observations well without considering this factor (see Section 4 for further discussion). Moreover, our simulation does not aim to replicate the exact acceleration mechanism that occurs at the shock wave. Rather, we assume that the particle distributions emitted from the shock, as described in Equation (1), are the outcome of the acceleration mechanism happening at the shock. Although the injected particles may undergo additional acceleration upon interacting with the CME shock wave during the simulation, this extra acceleration is minimal. This is because the particles' mean free path is not significantly reduced near the shock, which prevents them from being efficiently trapped close to the shock. As a result, an efficient DSA process does not take place in the current PARADISE simulation.

Figure 5 shows the divergence of $V_{\rm sw}$ in the solar equatorial plane as modeled by EUHFORIA, 23.75 hr after the insertion of the CME. Compression and shock waves in the solar wind can be easily identified with $\nabla \cdot V_{\rm sw}$, since these structures are characterized by converging flows and hence $\nabla \cdot V_{\rm sw} < 0$ (indicated by red, yellow, and blue colors in the figure). Figure 5 shows a leading forward shock (approaching the heliocentric distance of ~ 0.45 au) followed by a reverse shock. The formation of these two shocks is a consequence of the cone CME inserted in the EUHOFIRA simulation. Figure 5 illustrates that along the forward shock front, $\nabla \cdot V_{\rm sw}$ varies similarly to the gas compression ratio $r_{\rm g}$ shown in Figure 4(b). That is, the most negative $\nabla \cdot V_{\rm sw}$ values in the shock front can be seen in the regions indicated by (1) and (2) in Figure 5, which is where the slow wind is preceding and trailing the HSS, and where $r_{\rm g}$ is also enhanced. The correspondence

between $\nabla \cdot V_{\rm sw}$ and $r_{\rm g}$ is not surprising, since both quantities give a measure of the compression of the simulated shock front. Apart from the CME-driven shock waves, there are some standing compressive structures close to the inner boundary ($r < 0.15$ au), which arise from an imbalance in the total pressure (that is, magnetic and thermal pressure) at the inner boundary of EUHFORIA. In the PARADISE simulation, it is assumed for simplicity that Q is zero in these structures and particles are only emitted from the forward shock wave of the CME, from the time when it is injected at the inner boundary.

The normalization factor C in Equation (1) is fixed by requiring that the simulated particle intensities at the time of the shock arrival at ACE match the intensity in the 68–115 keV energy channel measured by the Low-Energy Magnetic Spectrometer 120 (LEMS120) of the Electron, Proton, and Alpha Monitor (EPAM; Gold et al. 1998) on board ACE. The energy spectrum between 115 keV and 4.8 MeV of the SEP fluence measured by LEMS120 between the first SEP intensity peak (2021 October 11 at 01:10 UT; see Figure 3(a)) and the arrival of the CME (2021 October 12 at 01:40 UT) can be fitted by a power law $E^{-\gamma}$, with $\gamma = 2.78$. According to steady-state DSA, the power-law index $\gamma = 2.78$ indicates that the compression ratio of the particle scattering centers across the shock, denoted as $r_{\rm sc}$, is 1.66. Assuming that the scattering centers are frozen into the solar wind plasma, we have $r_{\rm sc} = r_{\rm g}$. However, if the scattering centers are, for example, Alfvén waves, $r_{\rm sc}$ may differ from $r_{\rm g}$ (see, e.g., Vainio & Schlickeiser 1998, 1999). It is also important to note that the compression ratio varies with time and space (see Figure 4(b)), meaning that the energy power law observed at the shock crossing likely results from current and past acceleration conditions at the shock wave. In Equation (1), we inject a slightly softer power
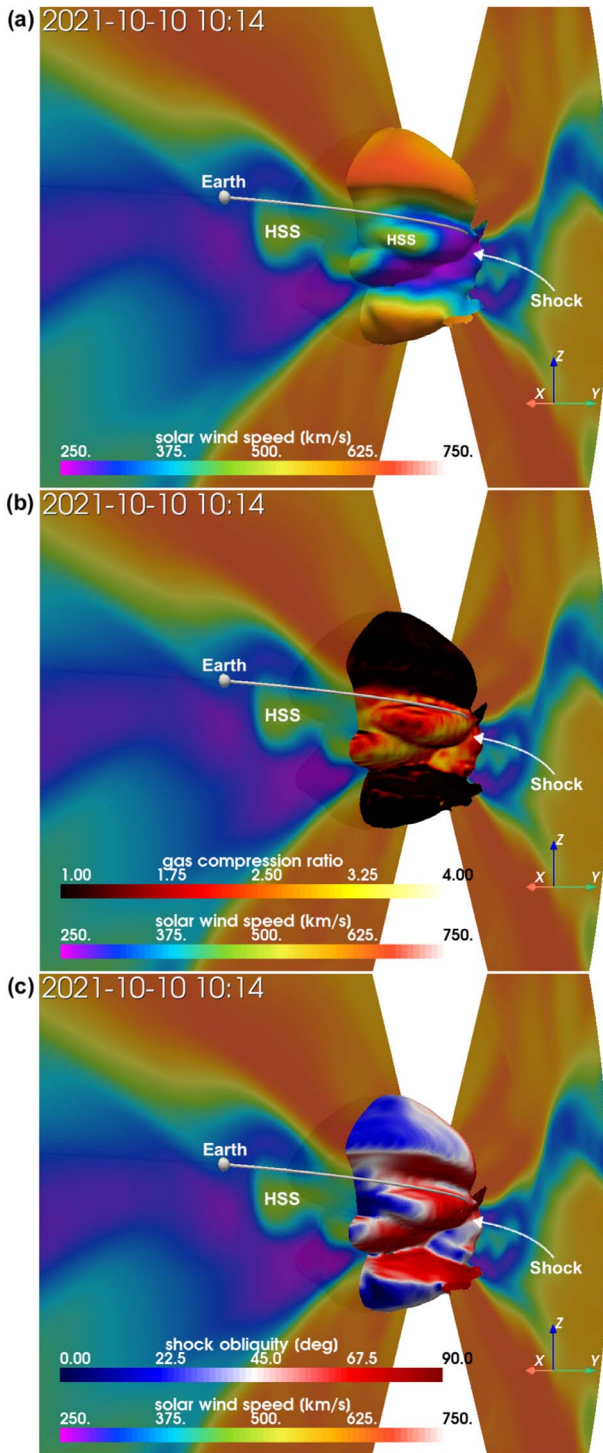
Figure 4. The CME-driven shock surface (occulting the Sun) together with a meridional slice color coded according to the solar wind speed. The magnetic field line connecting Earth with the shock surface is shown in white. In panel (a), the shock surface is color coded according to the upstream solar wind speed, in panel (b) according to the gas compression ratio r_g, and in panel (c) according to the shock obliquity θ_{B_n}. The panels correspond to the same time ($\sim$23.75 hr after the insertion of the CME) and capture the shock when its nose was at $\sim$0.45 au.

Figure 5. The divergence of the modeled solar wind velocity in the solar equatorial plane, centered on the CME, on 2021 October 10, 10:14 UT when the CME nose was at 0.45 au. The gray dashed semicircle indicates the heliocentric distance of 0.5 au. Labels (1) and (2) indicate the regions of highest $-\nabla \cdot \boldsymbol{V}_{sw}$.

In the following, we focus on the low-energy (<5 MeV) protons observed by Bepi and Earth only. As already commented, the EUHFORIA modeling domain starts at 0.1 au and therefore does not include particle acceleration and transport in the corona. This precludes modeling the SEP event as observed at Solar Orbiter, Parker Solar Probe, and STEREO-A adequately because these spacecraft observed a prompt onset (see Figures 7–9 in Lario et al. 2022), presumably due to the arrival of SEPs accelerated by the CME-driven shock when the CME was still below 0.1 au. We leave the inclusion of the shock at distances $r < 0.1$ au for future work.

3.2. Comparison between the Observations and the Simulations

Figure 6 shows the solar wind speed (panel a) and the simulated omnidirectional 321–580 keV proton intensities (panel b) in a latitudinal slice containing Earth, when the CME nose is at $\sim$0.45 au. The highest particle intensities are found in the regions indicated by (1) and (2) in the figure, that is, where the shock propagates through the slow wind preceding and trailing the HSS. These regions connect magnetically to the most compressive parts of the shock wave where the particle emission is the strongest (regions (1) and (2) indicated in Figure 5). In addition, we note that the particle intensities are higher in region (1) than in region (2), despite $|\nabla \cdot \boldsymbol{V}_{sw}|$, and thus Q, being slightly larger in region (2). This is because region (1) coincides with the SIR that is being driven by the HSS and the magnetic field compression inside the SIR causes the particles to propagate along a narrow path, leading to an enhancement of particle intensities in the elongated dark red band in region (1) in Figure 6(b).

Figure 3(a) shows the in situ observations made by ACE near Earth. In particular, the figure shows, from top to bottom, the energetic ion intensities from 68 keV to 4.80 MeV measured by EPAM/LEMS120, the IMF magnitude measured by the Magnetic Field Experiment (MAG; Smith et al. 1998), and the solar wind proton speed and density measured by the Solar Wind Electron Proton Alpha Monitor (SWEPAM; McComas et al. 1998) on ACE. As discussed by Lario et al. (2022), the energetic ion enhancement at ACE following the
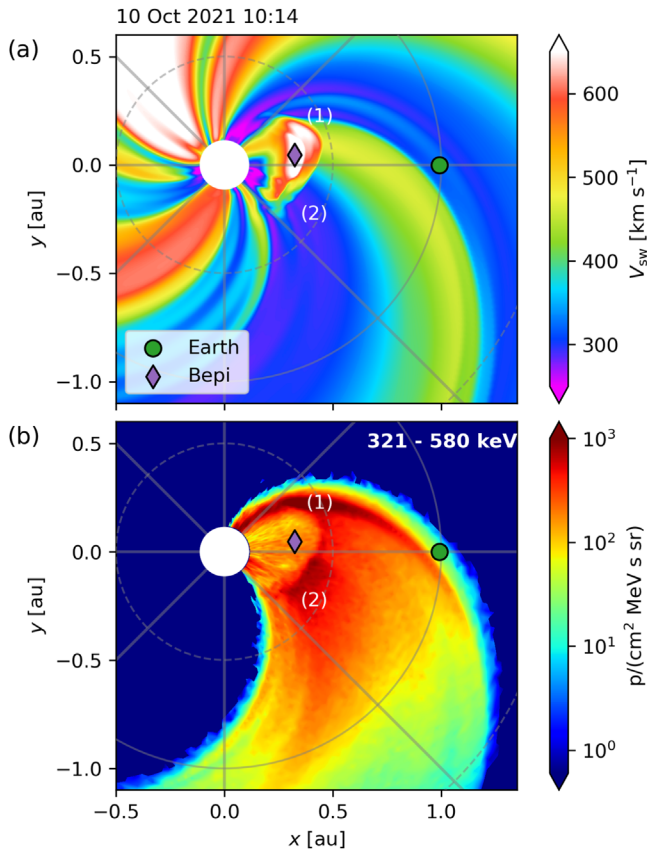
law E^{-3} than the one observed when the shock crosses ACE, since SEP transport processes tend to harden the observed energy spectra (e.g., Ruffolo 1995; Wijsen et al. 2020). The factor r^{-2} in Equation (1) takes into account the expansion of the solar wind into the heliosphere.

Figure 6. Panel (a) shows a snapshot of the modeled solar wind speed on 2021 October 10 at 10:14 UT when the CME nose was at a distance of 0.45 au. Panel (b) displays the modeled omnidirectional 321–580 keV proton intensities for the same time. Labels (1) and (2) indicate the regions of the highest particle intensities (see text for details). An animated version of this figure is available, showing the time evolution of the solar wind speed and the omnidirectional particle intensities. The video highlights the nonuniform particle intensities upstream and downstream of the shock wave. Throughout the simulation, the interaction between the SIR and the CME is observed to produce the highest intensities. The animation runs from 2021 October 9 10:54 to 2021 October 12 16:54, with a real-time duration of 16 s.

(An animation of this figure is available.)

solar event on 2021 October 9 was highly structured and the largest low-energy ion intensities occurred between passage of the SIR indicated in the figure and the shock marked by the solid vertical line. The ion intensities then dropped rapidly in the sheath between the shock and the ejecta of the ICME (gray shaded region).

Figure 3(b) shows the omnidirectional proton intensities modeled by PARADISE, together with the magnetic field magnitude, the solar wind speed, and the solar wind proton density modeled by EUHFORIA. Although the observed and modeled particle intensities have the same energy ranges, PARADISE considers only protons whereas EPAM/LEMS120 measures ions without distinguishing different species. Nevertheless, EPAM/LEMS120 measurements are in principle dominated by protons (Gold et al. 1998). Figure 3 shows that both EUHFORIA and PARADISE simulations successfully reproduce several features of the observed interplanetary medium and SEP event. In particular, the modeled intensity–time profiles show a first peak coinciding with the arrival of the SIR. This first peak corresponds to the intensity enhancement indicated by number (1) in Figure 6(b). After the first peak, the modeled intensities decrease slightly for the highest energy

channels ($\gtrsim$580 keV) and remain approximately constant for the lowest energy channels ($\lesssim$321 keV), in agreement with the observations. During this period of approximately flat $\lesssim$321 keV proton intensity–time profiles, the SIR is already beyond ACE, but the spacecraft remains immersed in the HSS and magnetically connected to the SIR at radial distances beyond 1 au. Since the SIR is characterized by a magnetic field enhancement, some outward propagating particles will be mirrored upon reaching the magnetic compression, eventually contributing to the quasi-constant intensities measured by ACE before the arrival of the CME.

The observed sheath region shows several fluctuations in the magnetic field and the proton density that are not captured by our MHD simulation. Both in the observations and in the simulation, the intensities decrease as the sheath passes the observer. In particular, the observed particle intensities decrease in two steps followed by an increase at around $\sim$ 05:00 UT on 2021 October 12 in the sheath prior to the arrival of the ejecta of the ICME (indicated by the gray shaded region). The sudden decrease in the observed ion intensities on entry to the ejecta (more prominent at energies $\lesssim$1 MeV) is also not reproduced by the simulations that show no change in the rate of the continuing intensity decay at entry into the ICME. This is mostly because the CME was simulated using a simple cone CME model instead of a more sophisticated magnetized CME model (such as the one used in Wijsen et al. 2022), making access of the particles into the ejecta easier than in the case of a closed magnetic field structure.

Next, we compare the in situ data and simulation results at Bepi, which was located at 0.33 au from the Sun and 2° west of Earth at the onset of the SEP event. The top panel of Figure 7 shows the modeled proton intensities (blue line) from PARADISE together with the count rates (orange line) measured in the 1.5–5.9 MeV proton channel of the BepiColombo Radiation Monitor (BERM; Pinto et al. 2022). The second panel of Figure 7 shows the magnetic field magnitude measured by the magnetometer on board Bepi's Mercury Planetary Orbiter (MPO-MAG; Heyner et al. 2021), together with the modeled magnetic field from EUHFORIA. The two bottom panels show the modeled solar wind speed and proton density; unfortunately, no solar wind plasma measurements from Bepi were available. In order to illustrate the qualitative match between the observed and the simulated SEP intensities, the modeled SEP and plasma time series presented in Figure 7 have been shifted backward in time by 4 hr (the reason for this shift is explained below). Both the simulated and the BERM intensity–time profiles display a two-peak structure prior to the arrival of the shock (indicated by the vertical solid line). In the simulation, the first peak is due to the arrival of SEPs accelerated in the interaction between the shock and the developing SIR (region (1) in Figures 5 and 6) where Bepi was connected to at the onset of the event. The second, longer-duration, increase is due to the approach of the CME-driven shock (i.e., the source of particles) to Bepi. The profiles do differ following the shock in that the modeled intensity falls rapidly whereas the observations show a further peak followed by an abrupt decrease on entry to the ICME ejecta (Lario et al. 2022).

We note that the correspondence between the modeled and observed magnetic field is not as good at Bepi as it was at ACE. The magnetic field modeled by EUHFORIA is not as structured as the observed one, which may explain why PARADISE
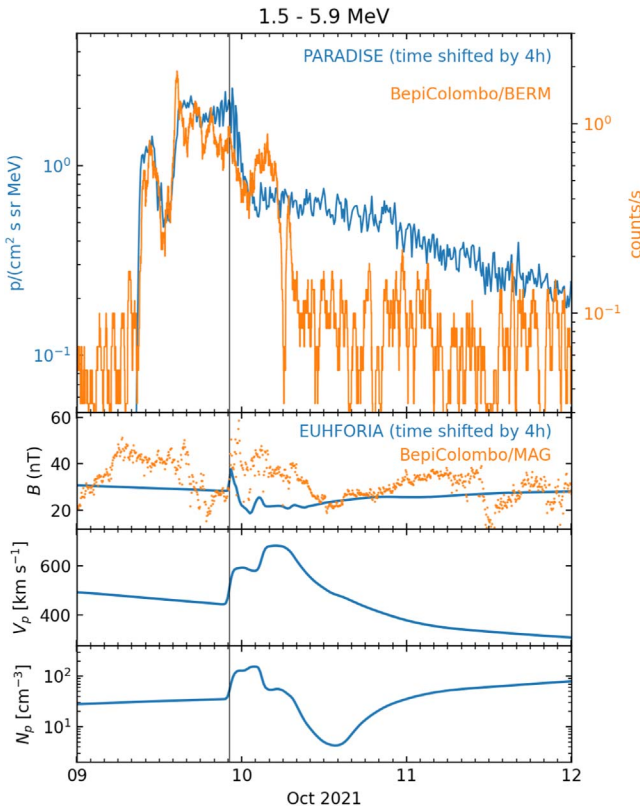
Figure 7. Observed (orange) and modeled (blue) SEP intensity and solar wind properties at Bepi. The PARADISE and EUHFORIA simulation results have been shifted 4 hr back in time to align with the observed shock. The top panel shows the modeled proton intensities together with the BERM ion counts in the energy bin 1.5–5.9 MeV. The second panel shows the observed and modeled magnetic field magnitude. The bottom two panels show the modeled solar wind speed and proton density.

misses the intensity peak occurring in the shock sheath. Furthermore, the magnetic compression observed at Bepi on 2021 October 9 is not reproduced. This magnetic compression was identified by Lario et al. (2022) as a likely candidate for the developing SIR associated with the HSS observed at ACE, whereas in the simulation, this HSS and the associated magnetic compression passes Bepi earlier, i.e., on 2021 October 8 (this is not shown in Figure 7, but easily seen in the movie accompanying Figure 2). Assuming that the magnetic compression seen early on 2021 October 9 at Bepi is indeed the same as the compression seen at ACE late on 2021 October 10, the solar wind must have been traveling at an average speed of ~800 km s^{-1} from Bepi to ACE, which is well above the observed speed at ACE. This discrepancy can most likely be attributed to the 4° of latitudinal separation between the spacecraft. That is, the coronal hole generating the HSS appeared slanted on the solar disk, extending increasingly westward toward lower latitudes (e.g., H1 in Figure 3(b) of Lario et al. 2022). Hence, if the HSS followed a similar spatial structure as its parent coronal hole, two spacecraft located at the same longitude but at different latitudes will see the HSS at different times, with the spacecraft at lower latitudes seeing the HSS earlier (even after adjusting for different helioradii). Moreover, latitudinal variations inside HSSs and the SIRs they drive are not uncommon, as illustrated by Jian et al. (2019) who analyzed 151 pairs of SIRs seen by STEREO-A and -B and showed that, even within 5° of latitude, the solar wind properties of a single SIR can vary strongly.

As mentioned before, the modeled time series presented in Figure 7 have been shifted back in time by 4 hr. That is, in the original EUHFORIA simulation, the CME shock arrived 4 hr too late at Bepi as compared to the observations. A discrepancy of 4 hr between observations and MHD heliospheric models such as EUHFORIA is not uncommon (e.g., Riley et al. 2018) and, in our case, may be largely due to the mismatch between the observed and simulated HSS at Bepi's latitude. That is, if the background solar wind is not well captured, the drag on the CME can be over or underestimated making the CME arrive too early or too late. An error on the assumed injection parameters of the CME and the simplicity of the cone model may also contribute to the 4 hr mismatch between the simulations and observations. Furthermore, we note that, depending on the width and the local expansion of the shock in the lower corona, the interaction between the shock wave and the HSS could have started below the inner boundary of our model, i.e., 0.1 au. Therefore, Bepi may have already established a magnetic connection to the shock before it crossed the 0.1 au boundary, which could contribute to the 4 hr discrepancy between the simulation and observation. Nonetheless, this does not alter the finding that the interaction between the SIR and the CME was most probably responsible for the distinct two-peak particle intensity pattern observed by Bepi.

4. Summary and Discussion

In this study, we present simulation results of the gradual SEP event observed on 2021 October 9 using the EUHFORIA and PARADISE models and compare these results with the multi-spacecraft observations of this event reported by Lario et al. (2022). In particular, we focus on understanding the unusual but similar low-energy (<5 MeV) proton intensity–time profiles measured at Bepi and ACE. According to Lario et al. (2022), these observations suggested that the proton intensities were strongly affected by the passage of a corotating high-speed solar wind stream prior to the arrival of the CME shock at both spacecraft. An important finding of this work is that the shock driven by the ICME was significantly deformed by the HSS, which led to strongly nonuniform shock conditions that might have changed the efficiency of particle acceleration along the shock front. In the model, it is assumed that the particle emission from the shock is proportional to the shock strength as measured by $\nabla \cdot V_{sw}$. The excellent agreement between the observed and simulated intensity–time profiles at both Earth and Bepi corroborates the results of the PARADISE simulation. The match can be attributed to the significant variations of the modeled shock strength, with the strongest particle emission originating from the regions of the shock propagating through the SIR and the slow wind.

Lario et al. (2022) hypothesized that the enhanced particle intensities observed at Earth and Bepi could have been the result of particles confined between the SIR and the approaching CME. Although such a transport process might have contributed to shaping the SEP event detected at Bepi and Earth, our modeling suggests that variations of the energetic particle emission at the CME-driven shock due to the shock interacting with the varying background solar wind, and in particular the SIR, may have played a dominant role. A similar explanation for another event was proposed by Ding et al. (2022), where the authors used the improved Particle Acceleration and Transport in the Heliosphere model (iPATH;

see Hu et al. 2017, and references therein) to study the SEP event on 2020 November 29, observed by Solar Orbiter, Parker Solar Probe, STEREO-A, and spacecraft near Earth and Mars (Kollhoff et al. 2021; Palmerio et al. 2022). The CME generating that event also interacted with a high-speed stream, and the authors likewise concluded that this interaction and the resulting deformation of the shock wave played an important role in the variation of time–intensity profiles measured at different spacecraft.

Another remarkable feature of the event studied in this work is that the HSS affecting the energetic particle profiles at Bepi and Earth was in fact quite modest. That is, near Earth, the solar wind speed only increased from $\sim$300 to 410 km s^{-1} during the passage of the HSS. The fact that an HSS with such a small speed increase can have a significant effect on the development of the CME shock and the associated SEP event further indicates the necessity of reliable solar wind models for considering the influence of solar wind structures on the event-to-event variability of SEP events. In addition, we note that CMEs in the EUHFORIA model are inserted at its inner boundary, located at 0.1 au. Thus, the strong deformation of the CME shock in our modeling is solely due to interactions between the CME and the solar wind beyond 0.1 au. However, shock waves can already become distorted in the corona below 0.1 au (e.g., Kwon et al. 2013). Such distortions are also expected to significantly alter the efficiency of particle acceleration along the shock front in the corona, below the starting height of the simulations presented in this work. Jebaraj et al. (2023) studied the low-coronal evolution of the same event and suggested that strong EUV wave deformations occurred due to the presence of several magnetic and density structures. Taking such deformations into account might help to improve the correlations found by Kouloumvakos et al. (2019) and Dresing et al. (2022) between the intensities of observed SEP events and certain shock properties, such as the shock obliquity, which the authors derived from fitting an ellipsoidal shock model to white-light coronagraph images. However, it is worth noting that our PARADISE simulation agrees well with the observations, without including an explicit relationship between the shock obliquity and the energetic particle emission from the shock (see Equation (1)). This despite that many particle acceleration mechanisms depend on the shock obliquity (see, e.g., Bell 1978; Ball & Melrose 2001; Chen et al. 2022). One possible explanation for the accuracy of our simulation is that small scale solar wind turbulence, which EUHFORIA does not account for, causes the shock obliquity to fluctuate significantly as the shock propagates through the solar wind (e.g., Richardson & Cane 2010). It is also worth mentioning that the SIR and CME shock interaction, which resulted in the initial peak of particle intensity profiles at Bepi and ACE, produced a predominantly quasi-perpendicular shock geometry throughout the event that could have created favorable conditions for efficient acceleration, if a rich suprathermal seed population was present and a small spatial diffusion coefficient perpendicular to the magnetic field increased the acceleration rate of particles (e.g., Jokipii 1987; Giacalone 2005a, 2005b; Chen et al. 2022).

Finally, we note that a good match between the SEP observations and simulations at Bepi was obtained after accounting for the 4 hr mismatch between the observed and simulated CME arrival times. The importance of bringing the simulated solar wind into agreement with observed solar wind

was also pointed out in Wijsen et al. (2021), where the authors modeled energetic particle enhancements produced by a SIR that was observed by both Parker Solar Probe (located at 0.56 au) and STEREO-A (near 1 au). As in the work presented here, a good agreement between the observed and simulated energetic particle intensities was only obtained once a mismatch between the modeled and simulated solar wind was taken into account. Thus, an important conclusion from these studies is that simulated energetic particle intensities typically tend to show a good agreement with observations only if the underlying solar wind is well captured by the modeling. This means that the reliability of any SEP forecasting tool that requires a model for the background solar wind is strongly dependent on the forecasting tool utilized for the underlying ambient medium.

ORCID iDs

Nicolas Wijsen ⓘ https://orcid.org/0000-0001-6344-6956
David Lario ⓘ https://orcid.org/0000-0002-3176-8704
Beatriz Sánchez-Cano ⓘ https://orcid.org/0000-0003-0277-3253

Immanuel C. Jebaraj ⓘ https://orcid.org/0000-0002-0606-7172
Nina Dresing ⓘ https://orcid.org/0000-0003-3903-4649
Ian G. Richardson ⓘ https://orcid.org/0000-0002-3855-3634
Angels Aran ⓘ https://orcid.org/0000-0003-1539-7832
Athanasios Kouloumvakos ⓘ https://orcid.org/0000-0001-6589-4509
Zheyi Ding ⓘ https://orcid.org/0000-0002-9829-3811
Antonio Niemela ⓘ https://orcid.org/0000-0002-3746-9246
Erika Palmerio ⓘ https://orcid.org/0000-0001-6590-3479
Fernando Carcaboso ⓘ https://orcid.org/0000-0003-1758-6194
Rami Vainio ⓘ https://orcid.org/0000-0002-3298-2067
Alexandr Afanasiev ⓘ https://orcid.org/0000-0001-9325-6758
Marco Pinto ⓘ https://orcid.org/0000-0002-5712-9396
Daniel Pacheco ⓘ https://orcid.org/0000-0002-6176-4077
Stefaan Poedts ⓘ https://orcid.org/0000-0002-1743-0651
Daniel Heyner ⓘ https://orcid.org/0000-0001-7894-8246

References

Ball, L., & Melrose, D. B. 2001, PASA, 18, 361
Bell, A. R. 1978, MNRAS, 182, 147
Benkhoff, J., Murakami, G., Baumjohann, W., et al. 2021, SSRv, 217, 90
Bieber, J. W., Dröge, W., Evenson, P. A., et al. 2002, ApJ, 567, 622
Bieber, J. W., Matthaeus, W. H., Smith, C. W., et al. 1994, ApJ, 420, 294
Cane, H. V., Reames, D. V., & von Rosenvinge, T. T. 1988, JGR, 93, 9555
Case, A. W., Spence, H. E., Owens, M. J., Riley, P., & Odstrcil, D. 2008, GeoRL, 35, L15105
Chen, X., Giacalone, J., & Guo, F. 2022, ApJ, 941, 23
Desai, M., & Giacalone, J. 2016, LRSP, 13, 3
Ding, Z., Wijsen, N., Li, G., & Poedts, S. 2022, A&A, 668, A71
Dresing, N., Kouloumvakos, A., Vainio, R., & Rouillard, A. 2022, ApJL, 925, L21
Drury, L. O., & Voelk, J. H. 1981, ApJ, 248, 344
Fox, N. J., Velli, M. C., Bale, S. D., et al. 2016, SSRv, 204, 7
Giacalone, J. 2005a, ApJ, 624, 765
Giacalone, J. 2005b, ApJL, 628, L37
Gold, R. E., Krimigis, S. M., Hawkins, S. E. I., et al. 1998, SSRv, 86, 541
Gopalswamy, N., Aguilar-Rodriguez, E., Yashiro, S., et al. 2005, JGRA, 110, A12S07
Heyner, D., Auster, H. U., Fornaçon, K. H., et al. 2021, SSRv, 217, 52
Hu, J., Li, G., Ao, X., Zank, G. P., & Verkhoglyadova, O. 2017, JGRA, 122, 10938
Jebaraj, I. C., Kouloumvakos, A., Dresing, N., et al. 2023, arXiv:2301.03650
Jian, L. K., Luhmann, J. G., Russell, C. T., & Galvin, A. B. 2019, SoPh, 294, 31
Jokipii, J. R. 1966, ApJ, 146, 480
Jokipii, J. R. 1987, ApJ, 313, 842
Kaiser, M. L., Kucera, T. A., Davila, J. M., et al. 2008, SSRv, 136, 5
Kallenrode, M. B., & Cliver, E. W. 2001, ICRC (Hamburg), 8, 3318
Kilpua, E. K. J., Fontaine, D., Good, S. W., et al. 2020, AnGeo, 38, 999

Kollhoff, A., Kouloumvakos, A., Lario, D., et al. 2021, A&A, 656, A20
Kouloumvakos, A., Kwon, R. Y., Rodríguez-García, L., et al. 2022, A&A, 660, A84
Kouloumvakos, A., Rouillard, A. P., Wu, Y., et al. 2019, ApJ, 876, 80
Kwon, R.-Y., Ofman, L., Olmedo, O., et al. 2013, ApJ, 766, 55
Lario, D., & Karelitz, A. 2014, JGRA, 119, 4185
Lario, D., Kwon, R.-Y., Riley, P., & Raouafi, N. E. 2017, ApJ, 847, 103
Lario, D., Wijsen, N., Kwon, R. Y., et al. 2022, ApJ, 934, 55
Lee, C. O., Luhmann, J. G., de Pater, I., et al. 2010, SoPh, 263, 239
Masson, S., Démoulin, P., Dasso, S., & Klein, K. L. 2012, A&A, 538, A32
McComas, D. J., Bame, S. J., Barker, P., et al. 1998, SSRv, 86, 563
Müller, D., Zouganelis, I., Cyr, O. C., St., Gilbert, H. R., & Nieves-Chinchilla, T. 2020, NatAs, 4, 205
Odstrcil, D., & Pizzo, V. J. 1999, JGR, 104, 28225
Owens, M. J., Lockwood, M., & Barnard, L. A. 2017, NatSR, 7, 4152
Palmerio, E., Kilpua, E. K. J., Witasse, O., et al. 2021, SpWea, 19, e2020SW002654
Palmerio, E., Lee, C. O., Mays, M. L., et al. 2022, SpWea, 20, e2021SW002993
Pinto, M., Sanchez-Cano, B., Moissl, R., et al. 2022, SSRv, 218, 54
Poedts, S., Lani, A., Scolini, C., et al. 2020, JSWSC, 10, 57
Pomoell, J., & Poedts, S. 2018, JSWSC, 8, A35
Prinsloo, P. L., Strauss, R. D., & Le Roux, J. A. 2019, ApJ, 878, 144
Reames, D. V. 1999, SSRv, 90, 413
Reames, D. V. 2009a, ApJ, 693, 812
Reames, D. V. 2009b, ApJ, 706, 844
Richardson, I. G. 2004, SSRv, 111, 267
Richardson, I. G. 2018, LRSP, 15, 1
Richardson, I. G., & Cane, H. V. 1996, JGR, 101, 27521
Richardson, I. G., & Cane, H. V. 2010, JGRA, 115, A07103
Riley, P., Mays, M. L., Andries, J., et al. 2018, SpWea, 16, 1245
Ruffolo, D. 1995, ApJ, 442, 861
Sarris, E. T., Anagnostopoulos, G. C., & Trochoutsos, P. C. 1984, SoPh, 93, 195
Savani, N. P., Owens, M. J., Rouillard, A. P., Forsyth, R. J., & Davies, J. A. 2010, ApJL, 714, L128
Scolini, C., Verbeke, C., Poedts, S., et al. 2018, SpWea, 16, 754
Smith, C. W., L'Heureux, J., Ness, N. F., et al. 1998, SSRv, 86, 613
Smith, C. W., Tessein, J. A., Vasquez, B. J., & Skoug, R. M. 2011, JGRA, 116, A10103
Smith, E. J. 2001, JGR, 106, 15819
Stone, E. C., Frandsen, A. M., Mewaldt, R. A., et al. 1998, SSRv, 86, 1
Vainio, R., & Schlickeiser, R. 1998, A&A, 331, 793
Vainio, R., & Schlickeiser, R. 1999, A&A, 343, 303
van den Berg, J., Strauss, D. T., & Effenberger, F. 2020, SSRv, 216, 146
Whitman, K., Egeland, R., Richardson, I. G., et al. 2022, AdSpR, 216, 146
Wijsen, N. 2020, PhD thesis, KU Leuven
Wijsen, N., Aran, A., Pomoell, J., & Poedts, S. 2019, A&A, 622, A28
Wijsen, N., Aran, A., Sanahuja, B., Pomoell, J., & Poedts, S. 2020, A&A, 634, A82
Wijsen, N., Aran, A., Scolini, C., et al. 2022, A&A, 659, A187
Wijsen, N., Samara, E., Aran, A. À., et al. 2021, ApJL, 908, L26
Wilson, L. B., Brosius, I., Gopalswamy, A. L., et al. 2021, RvGeo, 59, e2020RG000714
Zank, G. P., Li, G., Florinski, V., et al. 2006, JGRA, 111, A06108